


Rapid High-Fidelity Spin-State Readout in Si/Si-Ge Quantum Dots via rf Reflectometry

Elliot J. Connors^{✉,*}, JJ Nelson,[‡] and John M. Nichol^{✉,†}

Department of Physics and Astronomy, University of Rochester, Rochester, New York 14627, USA

 (Received 23 October 2019; revised manuscript received 19 November 2019; accepted 22 January 2020; published 10 February 2020)

Silicon spin qubits show great promise as a scalable qubit platform for fault-tolerant quantum computing. However, fast high-fidelity readout of charge and spin states, which is required for quantum error correction, has remained elusive. Radio-frequency reflectometry enables rapid high-fidelity readout of GaAs spin qubits, but the large capacitances between accumulation gates and the underlying two-dimensional electron gas in accumulation-mode Si quantum-dot devices, as well as the relatively low two-dimensional electron gas mobilities, have made radio-frequency reflectometry challenging in these platforms. In this work, we implement radio-frequency reflectometry in a Si/Si-Ge quantum-dot device with overlapping gates by making minor device-level changes that eliminate these challenges. We demonstrate charge-state readout with a fidelity above 99.9% in an integration time of 300 ns. We measure the singlet and triplet states of a double quantum dot via both conventional Pauli spin blockade and a charge latching mechanism, and we achieve maximum fidelities of 82.9 and 99.0% in 2.08- and 1.6- μ s integration times, respectively. We also use radio-frequency reflectometry to perform single-shot readout of single-spin states via spin-selective tunneling in microsecond-scale integration times.

DOI: [10.1103/PhysRevApplied.13.024019](https://doi.org/10.1103/PhysRevApplied.13.024019)

I. INTRODUCTION

Electron spins in gated Si quantum dots are promising qubits because they possess long coherence times, which enable high-fidelity gate operations [1–9]. In the future, quantum error correction will require a large number of physical qubits and the ability to measure and correct qubits quickly [10–12]. The fabrication of Si spin qubits leverages existing commercial technologies, and the production of large numbers of qubits seems within reach. Moreover, current architectures are compatible with one- and two-dimensional qubit arrays [13–15]. However, implementing readout methods that are simultaneously fast, high-fidelity, and scalable has been challenging in these systems.

Readout of electron spins in quantum dots is usually performed via spin-to-charge conversion together with an external charge sensor [6,13,16–21] or gate-based dispersive-sensing techniques [22–26]. Gate-based dispersive sensing does not require an additional charge sensor and is therefore inherently scalable, but it is often less sensitive than charge sensing. Charge sensing is easy to implement, sensitive, and compatible with linear qubit arrays, which have emerged as key elements of near-term spin-based quantum-information processors [13,27–29].

External charge sensors, such as quantum point contacts or quantum dots, can be used for both baseband or radio-frequency (rf) readout. In the former case, high-bandwidth baseband readout can be achieved, but it requires low-noise cryogenic preamplifiers and careful wiring to minimize stray capacitance [30,31]. In the latter case, rf reflectometry achieves high-bandwidth readout by incorporating the charge sensor into an impedance matching tank circuit [32–34]. Changes to the electrostatic potential of the charge sensor alter its conductance and therefore generate measurable changes to the reflection coefficient of the circuit. This technique enables fast and high-fidelity readout in GaAs quantum dots [33,35–37]. It is also easy to implement and enables frequency multiplexing for multiqubit readout.

Radio-frequency reflectometry has successfully been applied to Si donor-based devices [38,39]. However, accumulation-mode Si devices present two main challenges to rf reflectometry. First, accumulation-mode devices can incur sizeable capacitances of order 10^{-12} – 10^{-11} F if large-area accumulation gates are used. This is much larger than typical capacitances in reflectometry circuits, and it can negatively impact the performance of the tank circuit [34]. Second, Si devices often have lower mobilities than GaAs devices. These lower mobilities generate excess resistance in the two-dimensional electron gas (2DEG), diminishing the sensitivity of the charge sensor. Successful rf reflectometry circuits must be optimized such that both the incurred capacitance

*econnors@ur.rochester.edu

†john.nichol@rochester.edu

‡These authors contributed equally to this work.

and excess resistance are sufficiently small. For example, one cannot simply reduce the size of the accumulation gate arbitrarily, because that would increase the excess resistance. Previous work on rf reflectometry in silicon, including recent clever circuit modification strategies to circumvent the large capacitance [4,40–43], have shown promising results. However, rapid high-fidelity spin-state readout via rf reflectometry in silicon remains challenging.

Here, we implement high-fidelity charge- and spin-state sensing via rf reflectometry in a Si/Si-Ge quantum-dot device with overlapping gates. We eliminate the problems discussed above by making minor device-level changes. These changes are easy to implement and preserve the scalability of the overlapping-gate architecture. We demonstrate high-fidelity charge and singlet-triplet readout in submicrosecond integration times, and we use rf reflectometry to implement microsecond-scale single-spin readout.

II. DEVICE DESIGN

The quantum-dot devices in this report are fabricated on an undoped Si/Si-Ge heterostructure with an 8-nm-thick Si quantum well approximately 50 nm below the surface. Voltages applied to three overlapping layers of aluminum gates are used to confine electrons in up to four quantum dots [44,45] [Fig. 1(a)].

We optimize a quantum-dot device for rf reflectometry through the following design rules. First, the capacitance between the accumulation gate associated with the readout circuit and the 2DEG, C_G , should satisfy $C_G < 5 \times 10^{-14}$ F. Second, the total resistance of the path between the doped region associated with the readout circuit and the sensor dot, $R_T = \sum R_S$, should satisfy $R_T < 15R_S$, where R_S is the resistance per square of the 2DEG. Satisfying this condition likely ensures that $R_T \ll R_d$ for typical accumulation gate voltages and densities in Si/Si-Ge. Here R_d is the resistance of the sensor dot. We arrive at these empirical design rules by evaluating several prototype devices (Table I). As described below, the final device design has vastly reduced values of C_G and R_T compared to initial devices.

To accommodate these design rules, the n^{++} region in the reflectometry circuit extends to within 10 μm of the sensor dot, which helps to reduce R_T [Fig. 1(c)]. We use a screening gate [26], which runs underneath the accumulation gate associated with the reflectometry circuit, RA1, to reduce C_G as much as possible. Additionally, we remove the quantum well everywhere under RA1 except between the n^{++} region and the dot via a dry-etch process to ensure a minimization of C_G . The accumulation gate corresponding to the rf channel has a 12- μm^2 area consisting of roughly eight squares between the screening gate and the dot. The device has a 15-nm-thick Al_2O_3 gate-oxide layer and a 30-nm-thick Al_2O_3 field-oxide layer. While a thinner gate-oxide layer reduces charge noise [46], it increases C_G .

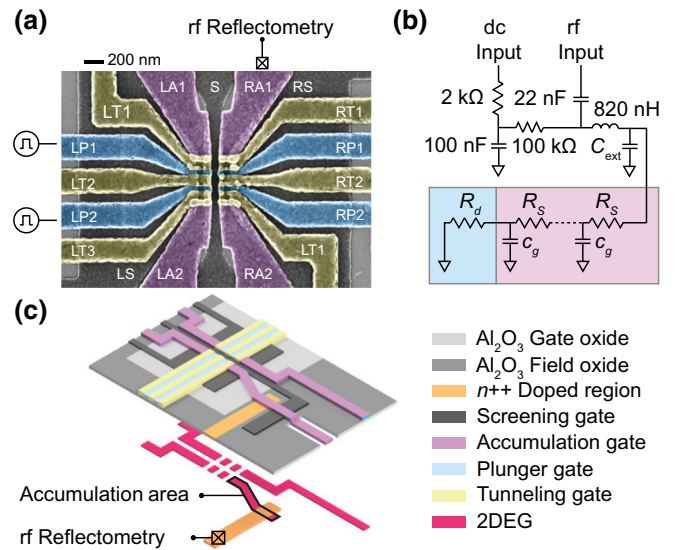


FIG. 1. Device and design. (a) False color scanning electron microscope image of a device with a nominally identical geometry to the ones tested. Gates are colored according to their purpose, with accumulation, screening, plunger, and tunneling gates shown in purple, black, blue, and yellow, respectively. The rf reflectometry circuit is connected to an Ohmic contact to the 2DEG indicated by a square with an “x” in it. (b) Schematic of the rf reflectometry circuit. The on-chip portion of the circuit is highlighted where the region in pink is the contribution from the 2DEG under the accumulation gate, and represents a distributed network of R_S and c_g components where $C_G = \sum c_g$ is the total gate capacitance. The region in blue is the contribution from the dot, and R_d is the resistance of the dot. (c) Schematic of the device used showing the underlying 2DEG formed in typical device operation. The accumulation area (outlined in black) is the region of the 2DEG that corresponds to the reflectometry circuit.

Although a matching capacitor can improve sensitivity of reflectometry in devices with large C_G [41], the large R_T , which is distributed with C_G , seems to prevent success with this approach in our devices. The device optimization described above represents a relatively simple method to implement rf reflectometry, and it should be widely applicable to most accumulation-mode Si quantum-dot devices.

The above-mentioned design criteria are evaluated in a prototype two-gate field effect transistor (FET), consisting of an accumulation gate spanning source and drain contacts and a depletion gate used to modulate the channel conductance. The relevant geometries of the FET device are designed to mimic the rf reflectometry circuit in a quantum-dot device. To evaluate the rf reflectometry performance, we cool the prototype device to approximately 4 K and measure S_{21} using a network analyzer connected to the device via a bias tee and directional coupler. For comparison, Fig. 2(a) shows the rf response of a quantum-dot device not optimized for rf reflectometry while 2(b)

TABLE I. Parameters and performance metrics of devices tested. Accumulation area is the area of the portion of the accumulation gate corresponding to the reflectometry circuit that accumulates a 2DEG beneath it and thus incurs a gate-to-2DEG capacitance, as shown in Fig. 1(c). N_S is the number of squares in the accumulation area. Sensitivity is the slope of the conductance peak used for charge sensing. We report here a typical achievable value of the sensitivity, and not the maximum value measured. $F_C(T_{\text{int}} = 1 \mu\text{s})$ is the charge-state readout fidelity as defined in Eq. (3) with an integration time $T_{\text{int}} = 1 \mu\text{s}$. QD 0 is a four quantum-dot device without any design optimization for rf reflectometry. QD 1, 2, and 3 are four quantum-dot devices at various iterations of rf reflectometry optimization. Measurements reported in Secs. III–V of this work are made on QD 3.

Device	Accumulation area (μm^2)	$N_S \left(\frac{d\text{DAQ}}{dV_{\text{RP1}}} \right)$	Sensitivity ($T_{\text{int}} = 1 \mu\text{s}$)	F_C
FET	~ 130	9
QD 0	~ 5000	~ 30	0	...
QD 1	83	11	5	...
QD 2	30	8	25	94.4%
QD 3	12	8	27	>99.9%

and 2(c) are the results of measurements performed on the FET. Figure 2(b) shows the response of the reflected signal to the accumulation gate voltage while using the depletion gate to fully suppress the channel conductance. The observed resonance is strongly affected by the gate voltage, demonstrating the capability of using an accumulation gate for *in situ* impedance matching. Once the circuit is matched via adjustments to the accumulation gate voltage, the reflected rf signal is sufficiently sensitive to changes in the channel conductance induced by the depletion gate [Fig. 2(c)]. A summary of relevant design parameters and performance metrics for select devices used to prototype the rf reflectometry optimization, including revisions of quantum-dot devices, is given in Table I. The design

rules and all results in the following sections pertain to device QD 3.

III. CHARGE-STATE READOUT

We cool our rf reflectometry optimized device (QD 3 in Table I) in a dilution refrigerator to a base temperature of approximately 50 mK and tune the gate voltages to form a sensor quantum dot under plunger gate RP1. We apply an rf excitation at 224 MHz to the Ohmic contact corresponding to RA1, which is part of the impedance-matching circuit. The rf carrier is generated at 10 dBm and sees 36, 20, and 13 dB of attenuation at room temperature, 1.5 K, and 50 mK, respectively. The circuit also consists of an

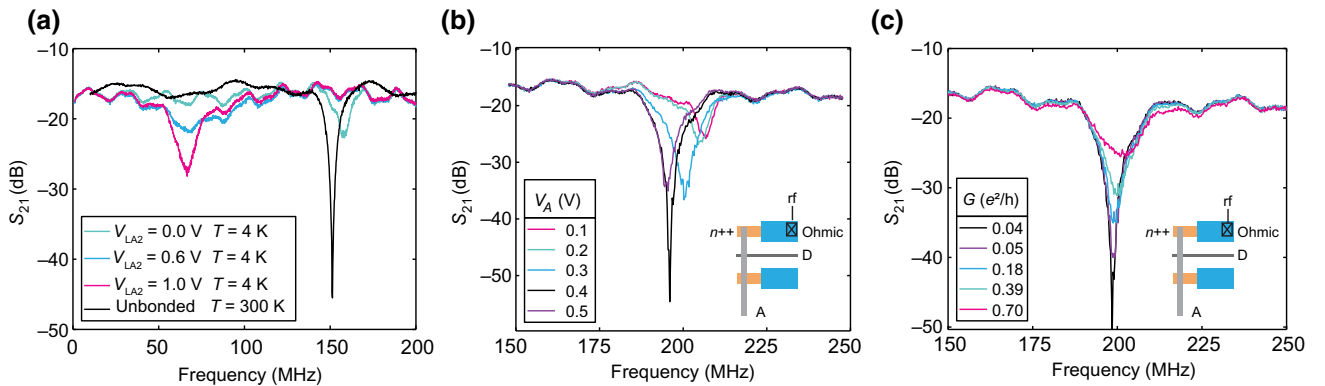


FIG. 2. Rf reflectometry performance in prototype devices. (a) Measurement of S_{21} in a quantum-dot device that is not optimized for rf reflectometry (QD 0) made using a network analyzer connected to the Ohmic contact corresponding to LA2 via a bias tee. The reflected rf signal is sensitive to the accumulation gate voltage, but no change is observed when the tunneling gates are used to modulate the channel conductivity. The large shift in the resonance frequency from approximately 150 MHz to approximately 70 MHz occurs when the accumulation gate is held above threshold thereby inducing a large C_G . (b) Demonstration of *in situ* impedance matching in a two-gate FET. V_A is the voltage on the accumulation gate (A) with the depletion gate (D) held below threshold. (c) Response of the reflected rf signal as the channel conductance is varied using the depletion gate. The -16 dB offset in (a)–(c) arises from the combination of room-temperature attenuation and amplification used on the send and return signals, respectively. The oscillations in the baseline arise from stray reflections in the measurement setup. The insets in (b) and (c) show a schematic of the two-gate FET tested. All measurements in (b) and (c) are made at approximately 4 K.

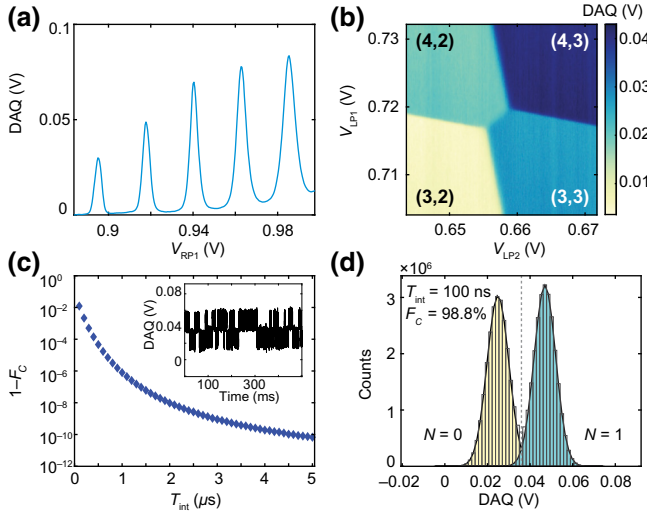


FIG. 3. Charge sensing via rf reflectometry. (a) Measurement of conductance peaks of the sensor dot using rf reflectometry. (b) Charge-stability diagram of a double quantum dot acquired via rf reflectometry measurement of the sensor dot. A plane has been subtracted to remove cross-talk between the double dot plunger gates and the sensor dot. (c) Plot of $1 - F_C$ as a function of integration time T_{int} . The inset shows a representative time series with $T_{\text{int}} = 300$ ns. (d) Histogram of the time series shown in (c) analyzed with an integration time $T_{\text{int}} = 100$ ns and having a measurement fidelity of $F_C = 98.8\%$.

820-nH surface mount inductor and the stray capacitance of the device, C_{ext} [Fig. 1(b)]. The reflected rf signal is amplified by 38 dB via a Cosmic Microwave Technologies CITLF3 cryogenic amplifier at approximately 4 K and an additional 54 dB via a Narda-MITEQ AU-1565 amplifier at room temperature before it is digitized on an AlazarTech ATS9440 data acquisition card (DAQ) [33]. During the tune-up process, we adjust the accumulation gate voltage, which affects both C_G and R_T , to optimize the sensitivity of the circuit [40]. We observe a strong modulation in the reflected signal as the plunger gate sweeps across conductance peaks [Fig. 3(a)].

To perform charge sensing, we set the plunger gate voltage to the side of a conductance peak such that the reflected rf signal is sensitive to small changes in the electrochemical potential of the dot. We then tune the gates on the left side of the device to form a double quantum dot, and acquire charge-stability diagrams by measuring the reflected rf signal while varying the voltages on plunger gates LP1 and LP2 [Fig. 3(b)].

We quantify the charge-state readout performance by tuning the left-side double dot to the (1,0) occupancy, where the (i,j) notation refers to the charge configuration with $i(j)$ electrons in the dot under gate LP1(LP2). We adjust the tunnel barrier coupling the dot under LP1 to its reservoir such that the tunneling rate is of order 10 Hz. We set the voltage of the plunger gate directly

on the (0,0)-(1,0) transition and acquire a time series of the reflected signal, and we resolve individual charge tunneling events [13] [Fig. 3(c)]. We fit a histogram of the data [Fig. 3(d)] to a function $G(V) = g(V|A_0, \mu_0, \sigma_0) + g(V|A_1, \mu_1, \sigma_1)$, where

$$g(V|A_i, \mu_i, \sigma_i) = \frac{A_i}{\sqrt{2\pi\sigma_i^2}} e^{-(V-\mu_i)^2/2\sigma_i^2} \quad (1)$$

is a Gaussian with amplitude, mean, and standard deviation A_i , μ_i , and σ_i , respectively. i indicates the occupation of the dot, and V is the measured voltage.

We define the measurement fidelity associated with occupation i as

$$f_{C,i} = \frac{\int_{V_s}^{V_f} g(V|A_i, \mu_i, \sigma_i) dV}{\int_{-\infty}^{\infty} g(V|A_i, \mu_i, \sigma_i) dV}. \quad (2)$$

The integral bounds in Eq. (2) are $V_s = -\infty$ and $V_f = V_t$ for $i = 0$, and $V_s = V_t$ and $V_f = \infty$ for $i = 1$, where V_t is the threshold voltage. V_t is chosen to maximize the charge-state readout fidelity

$$F_C = \frac{1}{2} (f_{C,0} + f_{C,1}). \quad (3)$$

Both V_t and F_C depend on the per-point integration time T_{int} . In our device, we achieve a charge-state readout fidelity of $F_C = 98.8\%$ and signal to noise ratio of $|\mu_1 - \mu_2| / \frac{(\sigma_1 + \sigma_2)}{2} = 4.3$ with an integration time as small as $T_{\text{int}} = 100$ ns [Fig. 3(d)]. By extending the integration time to just $T_{\text{int}} = 300$ ns, we achieve a charge-state readout fidelity $F_C > 99.9\%$ [Fig. 3(c)].

IV. SINGLET-TRIPLET READOUT

Having demonstrated fast high-fidelity charge sensing, we turn to fast readout of spin states. We observe Pauli spin blockade at the (4,2)-(3,3) transition in this device. (We did not observe spin blockade at the (1,1)-(0,2) transition, likely because of a small valley splitting.) We repeatedly apply a three-step pulse sequence that initializes a random spin state in (3,3) prior to pulsing toward the measurement point, at which point the rf excitation is applied to the sensor dot. When the randomly loaded spin state is a singlet, it can tunnel freely from (3,3) to (4,2). If it is a triplet, it remains blockaded in (3,3) until it either undergoes a spin flip or exchanges electrons with the reservoirs. We vary the position of the measurement point, and plot the average signal acquired at each measurement point in Fig. 4(a). A trapezoid indicating the spin-blockade region is visible in the (4,2) charge configuration near the interdot transition.

To quantify the singlet-triplet readout fidelity, we perform 10 000 single-shot measurements in which we initialize a random spin state before pulsing to the measurement point in the spin-blockade region, and an additional 10 000 measurements in which we instead preferentially initialize a singlet state prior to measurement. The two sequences described above pulse the gates between positions E, R, and M in Fig. 4(a), and positions E, R, L, and M, respectively. At the measurement point, we acquire a time series of the reflected rf signal for 40 μs for each single-shot measurement. The average difference between these signals as a function of measurement time from 0–40 μs is shown in Fig. 4(b). These data follow a characteristic exponential decay with a relaxation time $T_1 = 11.0 \mu\text{s}$. In fitting this data, we discard the first 2.5 μs of data at the

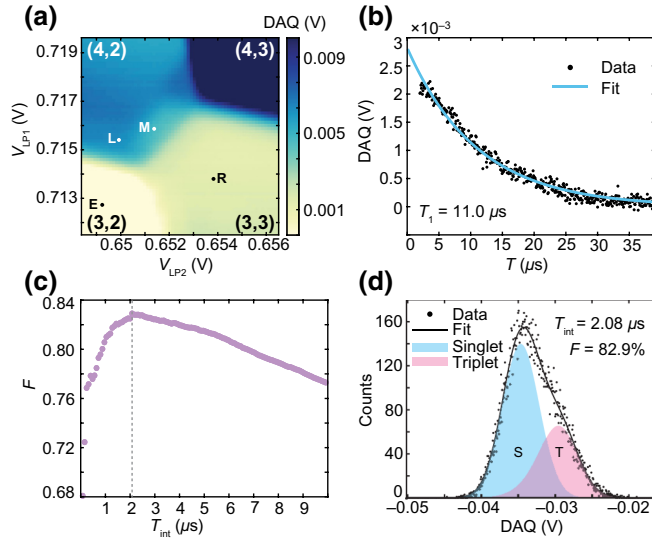


FIG. 4. Singlet-triplet readout via Pauli spin blockade. (a) Average charge-sensor signal acquired at each measurement point across many repetitions of a pulse sequence that initializes a random spin state prior to pulsing to the measurement point. A trapezoid near the interdot transition in the (4,2) charge configuration indicates the Pauli spin-blockade region. The limits of the color bar are adjusted such that the signal in the (4,3) and (3,2) charge configurations is saturated so that the spin-blockade region is more easily visible. Positions L, R, E, and M, are the ground-state initialization, random-state initialization, empty, and measure positions, respectively. (b) Difference of the average signals measured at position M after initializing a random state and after initializing a singlet state as a function of measurement time exhibiting a decay with $T_1 = 11.0 \mu\text{s}$. (c) Plot of the singlet-triplet readout fidelity as a function of integration time. A dashed line indicates the integration time at which the maximum fidelity is achieved. (d) Histogram of single-shot measurements with an integration time of $T_{\text{int}} = 2.08 \mu\text{s}$ and a fidelity of $F = 82.9\%$. The signal acquired on the DAQ is inverted from the signal shown in (a), resulting in the singlet states having the lower voltage signal. Data shown in (a)–(d) are taken at $B_{\text{ext}} = 50 \text{ mT}$, where B_{ext} is the externally applied in-plane magnetic field.

beginning of each measurement to allow for the circuit to ring up. The value of T_1 that we measure is lower than typical spin relaxation times in Si-based quantum dots [13]. This fast relaxation is likely related to the rf excitation and strong coupling between the dots and reservoirs in this device.

To compute a measurement fidelity, we use Eqs. (1)–(3) of Ref. [35] to fit a histogram of the data from the first pulse sequence discussed above to the sum of two noise broadened peaks with additional terms to account for relaxation [35]. We extract the readout fidelity as $F = \frac{1}{2}(F_S + F_T)$, where F_S and F_T are the singlet and triplet readout fidelities [35]. We choose the singlet-triplet threshold voltage to maximize the overall fidelity. Despite the enhanced triplet to singlet relaxation, we achieve a maximum fidelity of $F = 82.9\%$ in $T_{\text{int}} = 2.08 \mu\text{s}$ [Fig. 4(d)]. In this approach, we discard the first 500 ns of data to allow the resonator to ring up. The total measurement time is thus 2.58 μs . In computing the fidelity, we account for spin relaxation during this 500-ns interval.

To improve our readout fidelity, we use a charge latching mechanism [47–49]. We tune our device such that the tunneling rate between the dot under LP1 and its corresponding reservoir is $\Gamma_1 \sim 10 \text{ MHz}$ and the tunneling rate between the dot under LP2 and its corresponding reservoir is $\Gamma_2 \ll \Gamma_1$. In this tuning, we again apply a three-step pulse sequence that loads a random state prior to pulsing to the measurement point, and vary the measurement point [Fig. 5(a)]. The charge latching mechanism allows singlet states to tunnel across to (4,2), but triplet states instead preferentially tunnel to an excited charge state in (4,3). Generally, this technique results in better sensitivity than conventional spin-blockade readout, because the total electron number differs between these states.

We characterize the readout by performing 10 000 single-shot measurements at position M in Fig. 5(a) after initializing a random state by pulsing to positions E and then R, as well as after initializing a singlet state by pulsing to positions E, R, and then L. We observe a longer decay time of $T_1 = 51.9 \mu\text{s}$ [Fig. 5(b)], which is likely due to the reduced electron exchange rate with the reservoir connected to the double dot via the slow tunnel barrier. We compute the fidelity as before, but we now subtract an additional mapping error [49] $e_{\text{map}} = 1/T_{\text{int}} \int_{T_0}^{T_0+T_{\text{int}}} e^{-t/T_L} dt$. Here, $T_L \approx 150 \text{ ns}$ is the average tunneling time across the tunnel barrier connecting the dot under LP1 to its reservoir, and $T_0 = 650 \text{ ns}$ is the time we discard once the rf excitation is applied to allow the resonator to ring up and the latching process to take place. e_{map} is the average probability during the integration time that a triplet will not have tunneled to the (4,3) state and will be mistakenly identified as a singlet. Figure 5(c) shows the fidelity as a function of integration time for this method. We achieve a fidelity $F > 98\%$ with an integration time as short as $T_{\text{int}} = 800 \text{ ns}$ [Fig. 5(d)],

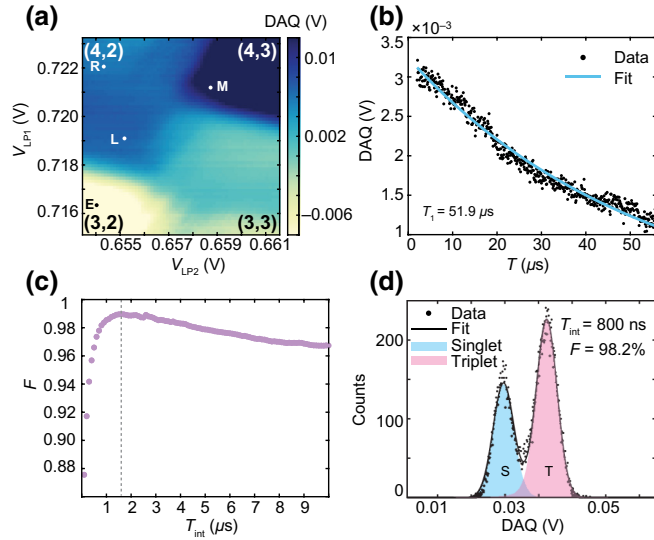


FIG. 5. Singlet-triplet readout utilizing a latching mechanism. (a) Average charge-sensor signal acquired at each measurement point across many repetitions of a pulse sequence that initializes a random spin state before pulsing to the measurement point. Positions L, R, E, and M, are the ground-state initialization, random-state initialization, empty, and measure positions, respectively. (b) Difference of the average signals measured at position M after initializing a random state and after initializing a singlet state as a function of measurement time exhibiting a decay with $T_1 = 51.9 \mu\text{s}$. (c) Singlet-triplet readout fidelity as a function of integration time. A dashed line indicates the integration time at which the maximum fidelity is achieved. (d) Histogram of single-shot measurements with an integration time of $T_{\text{int}} = 800 \text{ ns}$ and a fidelity of $F = 98.2\%$. Data shown in (a)–(d) are taken at $B_{\text{ext}} = 50 \text{ mT}$.

and an improved maximum fidelity of $F = 99.0\%$ in $T_{\text{int}} = 1.65 \mu\text{s}$ [Fig. 5(c)].

V. SINGLE-SPIN READOUT

Having demonstrated fast, high-fidelity singlet-triplet state readout, we now discuss fast single-spin readout via spin-selective tunneling [50]. Operating the device near the (0,0)–(1,0) transition and with $B_{\text{ext}} = 1.5 \text{ T}$, we apply a three-step pulse sequence [50] to plunger gate LP1, which empties and then loads the corresponding dot with a random spin, and then pulses to the measurement point [Fig. 6(a)]. At the measurement point, which is close to the (1,0)–(0,0) transition, a spin-up electron will preferentially tunnel out. Some time later, a spin-down electron will tunnel back in. This brief change in occupancy results in a measurable change in the charge-sensor signal.

We acquire more than 32 000 single-shot measurements using the pulse sequence described above. For each single-shot measurement, we additionally perform a control measurement using a pulse sequence in which we initialize

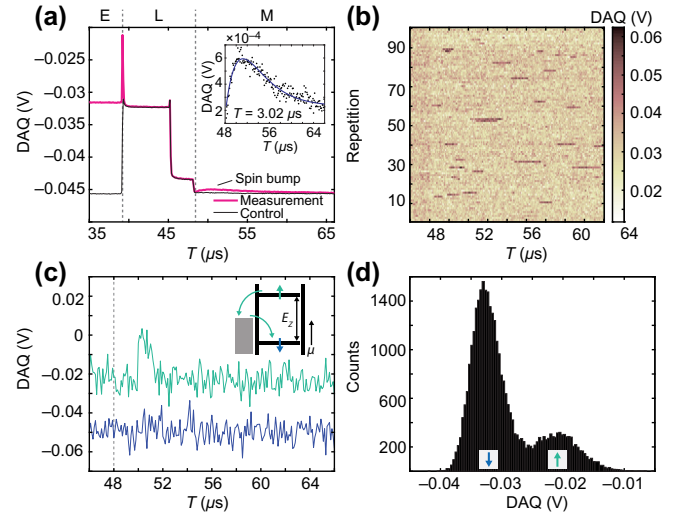


FIG. 6. Single-spin readout. (a) Averaged DAQ signal during the single-spin readout pulse sequence (pink). The sequence empties the dot, loads an electron with a random spin, and then pulses to the measurement point. Empty, load, and measurement sections of the pulse are separated by dashed gray lines, and are labeled with E, L, and M, respectively, above the plot. A spin bump corresponding to spin-up tunneling events is visible. A control pulse that initializes a spin-down electron prior to measurement is shown in black. The difference between the control and measurement pulses during the measurement window is shown in the inset. (b) 100 single-shot spin-selective tunneling events. The plunger gate is pulsed to the measurement point at $T = 48 \mu\text{s}$ in the pulse sequence. (c) Two representative single-shot traces. The top trace shows a spin-up electron tunneling out and back in as a spin down. The bottom trace shows no spike and indicates a spin-down electron. The traces are offset for clarity. (d) Histogram of the maximum single-point value of the signal in the range $T = 48 \mu\text{s}$ to $T = 66 \mu\text{s}$. Data shown in (a)–(d) are taken at $B_{\text{ext}} = 1.5 \text{ T}$ and a sampling rate of 10 MHz.

a spin-down electron instead of an electron with a random spin state. Figure 6(a) shows plots of the average acquired charge-sensor signal across all single-shot traces for both the measurement and control pulse sequences. A “spin bump” from the presence of tunneling events corresponding to spin-up electrons is visible at the beginning of the measurement window ranging from $T = 48\text{--}66 \mu\text{s}$. The signal from the control pulse shows no spin bump, as expected. The inset of Fig. 6(a) shows the difference between the average of the control and measurement pulse sequences in the measurement window. We fit these data to a function of the form $b(T) = A + B(T/\tau)e^{-T/\tau}$, where A , B , and τ are fit parameters, and T is the time from the start of the measurement window. We extract a characteristic tunneling time $\tau = 3.02 \mu\text{s}$. A representative collection of 100 single-shot traces is shown in Fig. 6(b), and two traces (one spin up and the other spin down) are shown in Fig. 6(c).

Figure 6(d) shows a histogram of the maximum single point value acquired in each single-shot measurement during the measurement window. This histogram shows two distinct peaks corresponding to spin-up and spin-down electrons. The overall acquisition time for each single-shot measurement is only 18 μ s, orders of magnitude faster than usual spin-selective tunneling measurement times [50]. This increase in speed is enabled by the high bandwidth of the reflectometry circuit.

VI. CONCLUSION

We optimize a Si/Si-Ge quantum-dot device with overlapping gates for rf reflectometry by making only modest geometric changes to our device design. The methods we use are applicable to Si devices with and without overlapping gates, can be implemented with relative ease, preserve the scalability of the gate layout, and, importantly, provide the ability to perform rapid high-fidelity charge and spin-state readout. We demonstrate microsecond-scale readout of single-spin states and submicrosecond singlet-triplet readout. We expect that further improvements are possible via optimization of the dot-reservoir couplings and the sensor dot position. This work presents a feasible solution to achieving rapid and high-fidelity spin-state readout in Si spin qubits that is largely compatible with existing device designs.

During the completion of this Paper, we became aware of a related result demonstrating similar techniques for the implementation of rf reflectometry in accumulation mode Si devices [51].

ACKNOWLEDGMENTS

We thank Aaron Mitchell Jones for valuable discussions. We thank Lisa F. Edge of HRL Laboratories, LLC. for the epitaxial growth of the Si-Ge material. Research is sponsored by the Army Research Office and is accomplished under Grants No. W911NF-16-1-0260 and No. W911NF-19-1-0167. The views and conclusions contained in this document are those of the authors and should not be interpreted as representing the official policies, either expressed or implied, of the Army Research Office or the U.S. Government. The U.S. Government is authorized to reproduce and distribute reprints for Government purposes notwithstanding any copyright notation herein. E.J.C. is supported by ARO and LPS through the QuaCGR Fellowship Program.

[1] M. Veldhorst, J. C. C. Hwang, C. H. Yang, A. W. Leenstra, Bob de Ronde, J. P. Dehollain, J. T. Muhonen, F. E. Hudson, Kohei M. Itoh, A. Morello *et al.*, An addressable

quantum dot qubit with fault-tolerant control-fidelity, *Nat. Nanotechnol.* **9**, 981 (2014).

- [2] Alexei M. Tyryshkin, Shinichi Tojo, John J. L. Morton, Helge Riemann, Nikolai V. Abrosimov, Peter Becker, Hans-Joachim Pohl, Thomas Schenkel, Michael L. W. Thewalt, Kohei M. Itoh *et al.*, Electron spin coherence exceeding seconds in high-purity silicon, *Nat. Mater.* **11**, 143 (2012).
- [3] Andrea Morello, Jarryd J. Pla, Floris A. Zwanenburg, Kok W. Chan, Kuan Y. Tan, Hans Huebl, Mikko Möttönen, Christopher D. Nugroho, Changyi Yang, Jessica A. van Donkelaar *et al.*, Single-shot readout of an electron spin in silicon, *Nature* **467**, 687 (2010).
- [4] Jun Yoneda, Kenta Takeda, Tomohiro Otsuka, Takashi Nakajima, Matthieu R. Delbecq, Giles Allison, Takumu Honda, Tetsuo Kodera, Shunri Oda, Yusuke Hoshi *et al.*, A quantum-dot spin qubit with coherence limited by charge noise and fidelity higher than 99.9%, *Nat. Nanotechnol.* **13**, 102 (2018).
- [5] Kevin Eng, Thaddeus D. Ladd, Aaron Smith, Matthew G. Borselli, Andrey A. Kiselev, Bryan H. Fong, Kevin S. Holabird, Thomas M. Hazard, Biqin Huang, Peter W. Deelman *et al.*, Isotopically enhanced triple-quantum-dot qubit, *Sci. Adv.* **1**, e1500214 (2015).
- [6] Brett M. Maune, Matthew G. Borselli, Biqin Huang, Thaddeus D. Ladd, Peter W. Deelman, Kevin S. Holabird, Andrey A. Kiselev, Ivan Alvarado-Rodriguez, Richard S. Ross, Adele E. Schmitz *et al.*, Coherent singlet-triplet oscillations in a silicon-based double quantum dot, *Nature* **481**, 344 (2012).
- [7] T. F. Watson, S. G. J. Philips, Erika Kawakami, D. R. Ward, Pasquale Scarlino, Menno Veldhorst, D. E. Savage, M. G. Lagally, Mark Friesen, S. N. Coppersmith *et al.*, A programmable two-qubit quantum processor in silicon, *Nature* **555**, 633 (2018).
- [8] Menno Veldhorst, C. H. Yang, J. C. C. Hwang, W. Huang, J. P. Dehollain, J. T. Muhonen, S. Simmons, A. Laucht, F. E. Hudson, Kohei M. Itoh *et al.*, A two-qubit logic gate in silicon, *Nature* **526**, 410 (2015).
- [9] X. Xue, T. F. Watson, J. Helsen, Daniel R. Ward, Donald E. Savage, Max G. Lagally, Susan N. Coppersmith, M. A. Eriksson, S. Wehner, and L. M. K. Vandersypen, Benchmarking Gate Fidelities in a Si/SiGe Two-Qubit Device, *Phys. Rev. X* **9**, 021011 (2019).
- [10] Lieven M. K. Vandersypen and Mark A. Eriksson, Quantum computing with semiconductor spins, *Phys. Today* **72**(8), 38 (2019).
- [11] Xin Zhang, Hai-Ou Li, Gang Cao, Ming Xiao, Guang-Can Guo, and Guo-Ping Guo, Semiconductor quantum computation, *Natl. Sci. Rev.* **6**, 32 (2018).
- [12] Austin G. Fowler, Matteo Mariantoni, John M. Martinis, and Andrew N. Cleland, Surface codes: Towards practical large-scale quantum computation, *Phys. Rev. A* **86**, 032324 (2012).
- [13] D. M. Zajac, T. M. Hazard, Xiao Mi, E. Nielsen, and J. R. Petta, Scalable Gate Architecture for a One-Dimensional Array of Semiconductor Spin Qubits, *Phys. Rev. Appl.* **6**, 054013 (2016).
- [14] Pierre-Andre Mortemousque, Emmanuel Chanrion, Baptiste Jadot, Hanno Flentje, Arne Ludwig, Andreas D. Wieck, Matias Urdampilleta, Christopher Bauerle, and

- Tristan Meunier, Coherent control of individual electron spins in a two dimensional array of quantum dots, arXiv:1808.06180 (2018).
- [15] Uditendu Mukhopadhyay, Juan Pablo Dehollain, Christian Reichl, Werner Wegscheider, and Lieven M. K. Vandersypen, A 2×2 quantum dot array with controllable inter-dot tunnel couplings, *Appl. Phys. Lett.* **112**, 183505 (2018).
- [16] C. B. Simmons, J. R. Prance, B. J. Van Bael, Teck Seng Koh, Zhan Shi, D. E. Savage, M. G. Lagally, R. Joynt, Mark Friesen, S. N. Coppersmith, and M. A. Eriksson, Tunable Spin Loading and T_1 of a Silicon Spin Qubit Measured by Single-Shot Readout, *Phys. Rev. Lett.* **106**, 156804 (2011).
- [17] Madhu Thalakulam, C. B. Simmons, B. J. Van Bael, B. M. Rosemeyer, D. E. Savage, M. G. Lagally, Mark Friesen, S. N. Coppersmith, and M. A. Eriksson, Single-shot measurement and tunnel-rate spectroscopy of a Si/SiGe few-electron quantum dot, *Phys. Rev. B* **84**, 045307 (2011).
- [18] M. Field, C. G. Smith, M. Pepper, D. A. Ritchie, J. E. F. Frost, G. A. C. Jones, and D. G. Hasko, Measurements of Coulomb Blockade with a Noninvasive Voltage Probe, *Phys. Rev. Lett.* **70**, 1311 (1993).
- [19] J. M. Elzerman, R. Hanson, J. S. Greidanus, L. H. Willems van Beveren, S. De Franceschi, L. M. K. Vandersypen, S. Tarucha, and L. P. Kouwenhoven, Few-electron quantum dot circuit with integrated charge read out, *Phys. Rev. B* **67**, 161308 (2003).
- [20] Jarryd J. Pla, Kuan Y. Tan, Juan P. Dehollain, Wee H. Lim, John J. L. Morton, David N. Jamieson, Andrew S. Dzurak, and Andrea Morello, A single-atom electron spin qubit in silicon, *Nature* **489**, 541 (2012).
- [21] M. A. Broome, T. F. Watson, D. Keith, S. K. Gorman, M. G. House, J. G. Keizer, S. J. Hile, W. Baker, and M. Y. Simmons, High-Fidelity Single-Shot Singlet-Triplet Readout of Precision-Placed Donors in Silicon, *Phys. Rev. Lett.* **119**, 046802 (2017).
- [22] J. I. Colless, A. C. Mahoney, J. M. Hornibrook, A. C. Doherty, H. Lu, A. C. Gossard, and D. J. Reilly, Dispersive Readout of a Few-Electron Double Quantum Dot with Fast rf Gate Sensors, *Phys. Rev. Lett.* **110**, 046805 (2013).
- [23] P. Pakkiam, A. V. Timofeev, M. G. House, M. R. Hogg, T. Kobayashi, M. Koch, S. Rogge, and Michelle Y. Simmons, Single-Shot Single-Gate rf Spin Readout in Silicon, *Phys. Rev. X* **8**, 041032 (2018).
- [24] Guoji Zheng, Nodar Samkharadze, Marc L. Noordam, Nima Kalhor, Delphine Brousse, Amir Sammak, Giordano Scappucci, and Lieven M. K. Vandersypen, Rapid gate-based spin read-out in silicon using an on-chip resonator, *Nat. Nanotechnol.* **14**, 742 (2019).
- [25] Matias Urdampilleta, David J. Niegemann, Emmanuel Chanrion, Baptiste Jadot, Cameron Spence, Pierre-André Mortemousque, Christopher Bäuerle, Louis Hutin, Benoit Bertrand, Sylvain Barraud, Romain Maurand, Marc Sanquer, Xavier Jehl, Silvano De Franceschi, Maud Vinet, and Tristan Meunier, Gate-based high fidelity spin readout in a cmos device, *Nat. Nanotechnol.* **14**, 737 (2019).
- [26] Anderson West, Bas Hensen, Alexis Jouan, Tuomo Tantt, Chih-Hwan Yang, Alessandro Rossi, M. Fernando Gonzalez-Zalba, Fay Hudson, Andrea Morello, David J. Reilly *et al.*, Gate-based single-shot readout of spins in silicon, *Nat. Nanotechnol.* **14**, 437 (2019).
- [27] C. Volk, A. M. J. Zwerver, U. Mukhopadhyay, P. T. Eendebak, C. J. van Diepen, J. P. Dehollain, T. Hensgens, T. Fujita, C. Reichl, W. Wegscheider, and L. M. K. Vandersypen, Loading a quantum-dot based “qubyte” register, *npj Quantum Inf.* **5**, 29 (2019).
- [28] Yadav P. Kandel, Haifeng Qiao, Saeed Fallahi, Geoffrey C. Gardner, Michael J. Manfra, and John M. Nichol, Coherent spin-state transfer via heisenberg exchange, *Nature* **573**, 553 (2019).
- [29] Haifeng Qiao, Yadav P. Kandel, Sreenath K. Manikandan, Andrew N. Jordan, Saeed Fallahi, Geoffrey C. Gardner, Michael J. Manfra, and John M. Nichol, Conditional teleportation of quantum-dot spin states, arXiv:1908.08306 (2019).
- [30] I. T. Vink, T. Nooitgedagt, R. N. Schouten, L. M. K. Vandersypen, and Werner Wegscheider, Cryogenic amplifier for fast real-time detection of single-electron tunneling, *Appl. Phys. Lett.* **91**, 123512 (2007).
- [31] A. M. Jones, E. J. Pritchett, E. H. Chen, T. E. Keating, R. W. Andrews, J. Z. Blumoff, L. A. De Lorenzo, K. Eng, S. D. Ha, A. A. Kiselev, S. M. Meenehan, S. T. Merkel, J. A. Wright, L. F. Edge, R. S. Ross, M. T. Rakher, M. G. Borselli, and A. Hunter, Spin-Blockade Spectroscopy of Si/Si-Ge Quantum Dots, *Phys. Rev. Appl.* **12**, 014026 (2019).
- [32] R. J. Schoelkopf, P. Wahlgren, A. A. Kozhevnikov, P. Delsing, and D. E. Prober, The radio-frequency single-electron transistor (rf-set): A fast and ultrasensitive electrometer, *Science* **280**, 1238 (1998).
- [33] D. J. Reilly, C. M. Marcus, M. P. Hanson, and A. C. Gossard, Fast single-charge sensing with a rf quantum point contact, *Appl. Phys. Lett.* **91**, 162101 (2007).
- [34] L. J. Taskinen, R. P. Starrett, T. P. Martin, A. P. Micolich, A. R. Hamilton, M. Y. Simmons, D. A. Ritchie, and M. Pepper, Radio-frequency reflectometry on large gated two-dimensional systems, *Rev. Sci. Instrum.* **79**, 123901 (2008).
- [35] Christian Barthel, D. J. Reilly, Charles Masamed Marcus, M. P. Hanson, and A. C. Gossard, Rapid Single-Shot Measurement of a Singlet-Triplet Qubit, *Phys. Rev. Lett.* **103**, 160503 (2009).
- [36] Christian Barthel, Morten Kjærgaard, J. Medford, M. Stopa, Charles Masamed Marcus, M. P. Hanson, and Arthur C. Gossard, Fast sensing of double-dot charge arrangement and spin state with a radio-frequency sensor quantum dot, *Phys. Rev. B* **81**, 161308 (2010).
- [37] Andrew Patrick Higginbotham, Ferdinand Kuemmeth, Micah P. Hanson, Arthur C. Gossard, and Charles M. Marcus, Coherent Operations and Screening in Multielectron Spin Qubits, *Phys. Rev. Lett.* **112**, 026801 (2014).
- [38] B. J. Willis, A. O. Orlov, S. Barraud, M. Vinet, M. Sanquer, P. Fay, G. Snider, and X. Jehl, Direct detection of a transport-blocking trap in a nanoscaled silicon single-electron transistor by radio-frequency reflectometry, *Appl. Phys. Lett.* **104**, 233503 (2014).
- [39] Samuel J. Hile, Matthew G. House, Eldad Peretz, Jan Verduijn, Daniel Widmann, Takashi Kobayashi, Sven Rogge,

- and Michelle Y. Simmons, Radio frequency reflectometry and charge sensing of a precision placed donor in silicon, *Appl. Phys. Lett.* **107**, 093504 (2015).
- [40] S. J. Angus, A. J. Ferguson, A. S. Dzurak, and R. G. Clark, A silicon radio-frequency single electron transistor, *Appl. Phys. Lett.* **92**, 112103 (2008).
- [41] N. Ares, F. J. Schupp, A. Mavalankar, G. Rogers, J. Griffiths, G. A. C. Jones, I. Farrer, D. A. Ritchie, C. G. Smith, A. Cottet, G. A. D. Briggs, and E. A. Laird, Sensitive Radio-Frequency Measurements of a Quantum Dot by Tuning to Perfect Impedance Matching, *Phys. Rev. Appl.* **5**, 034011 (2016).
- [42] K. Wang, C. Payette, Y. Dovzhenko, P. W. Deelman, and Jason R. Petta, Charge Relaxation in a Single-Electron Si/SiGe Double Quantum Dot, *Phys. Rev. Lett.* **111**, 046801 (2013).
- [43] Christian Volk, Anasua Chatterjee, Fabio Ansaloni, Charles M. Marcus, and Ferdinand Kuemmeth, Fast charge sensing of Si/SiGe quantum dots via a high-frequency accumulation gate, *Nano Lett.* **19**, 5628 (2019).
- [44] Susan J. Angus, Andrew J. Ferguson, Andrew S. Dzurak, and Robert G. Clark, Gate-defined quantum dots in intrinsic silicon, *Nano Lett.* **7**, 2051 (2007).
- [45] D. M. Zajac, T. M. Hazard, X. Mi, K. Wang, and J. R. Petta, A reconfigurable gate architecture for Si/SiGe quantum dots, *Appl. Phys. Lett.* **106**, 223507 (2015).
- [46] Elliot J. Connors, J. J. Nelson, Haifeng Qiao, Lisa F. Edge, and John M. Nichol, Low-frequency charge noise in Si/SiGe quantum dots, *Phys. Rev. B* **100**, 165305 (2019).
- [47] S. A. Studenikin, J. Thorgrimson, G. C. Aers, A. Kam, P. Zawadzki, Z. R. Wasilewski, A. Bogan, and A. S. Sachrajda, Enhanced charge detection of spin qubit readout via an intermediate state, *Appl. Phys. Lett.* **101**, 233101 (2012).
- [48] J. D. Mason, S. A. Studenikin, A. Kam, Z. R. Wasilewski, A. S. Sachrajda, and J. B. Kycia, Role of metastable charge states in a quantum-dot spin-qubit readout, *Phys. Rev. B* **92**, 125434 (2015).
- [49] Patrick Harvey-Collard, Benjamin D'Anjou, Martin Rudolph, N. Tobias Jacobson, Jason Dominguez, Gregory A. Ten Eyck, Joel R. Wendt, Tammy Pluym, Michael P. Lilly, William A. Coish *et al.*, High-Fidelity Single-Shot Readout for a Spin Qubit via an Enhanced Latching Mechanism, *Phys. Rev. X* **8**, 021046 (2018).
- [50] J. M. Elzerman, R. Hanson, L. H. Willems Van Beveren, B. Witkamp, L. M. K. Vandersypen, and Leo P. Kouwenhoven, Single-shot read-out of an individual electron spin in a quantum dot, *Nature* **430**, 431 (2004).
- [51] Akito Noiri, Kenta Takeda, Jun Yoneda, Takashi Nakajima, Tetsuo Kodera, and Seigo Tarucha, Radio-frequency detected fast charge sensing in undoped silicon quantum dots, *arXiv:1910.03282*.